



PAPER

Investigation of out-of-plane motion artifacts in 2D noninvasive vascular ultrasound elastography

RECEIVED
18 June 2018REVISED
8 November 2018ACCEPTED FOR PUBLICATION
14 November 2018PUBLISHED
10 December 2018Hongliang Li^{1,2}, Boris Chayer¹, Marie-Hélène Roy Cardinal¹, Judith Muijsers³, Marcel van den Hoven³, Zhao Qin¹, Marc Gesnik¹, Gilles Soulez^{2,4,5}, Richard G P Lopata³ and Guy Cloutier^{1,2,4}¹ Laboratory of Biorheology and Medical Ultrasonics, University of Montreal Hospital Research Center (CRCHUM), Montréal, QC, Canada² Institute of Biomedical Engineering, University of Montreal, Montréal, QC, Canada³ Department of Biomedical Engineering, Cardiovascular Biomechanics, Eindhoven University of Technology, Eindhoven, Netherlands⁴ Department of Radiology, Radio-Oncology and Nuclear Medicine, University of Montreal, Montréal, QC, Canada⁵ Department of Radiology, University of Montreal Hospital, Montréal, QC, CanadaE-mail: guy.cloutier@umontreal.ca**Keywords:** ultrasound elastography, carotid artery, carotid bifurcation phantom, mimicking artery plaque, out-of-plane motion artifact, carotid atherosclerotic plaques**Abstract**

Ultrasound noninvasive vascular elastography (NIVE) has shown its potential to measure strains of carotid arteries to predict plaque instability. When two-dimensional (2D) strain estimation is performed, either in longitudinal or cross-sectional view, only in-plane motions are considered. The motions in elevation direction (i.e. perpendicular to the imaging plane), can induce estimation artifacts affecting the accuracy of 2D NIVE. The influence of such out-of-plane motions on the performance of axial strain and axial shear strain estimations has been evaluated in this study. For this purpose, we designed a diseased carotid bifurcation phantom with a 70% stenosis and an *in vitro* experimental setup to simulate orthogonal out-of-plane motions of 1 mm, 2 mm and 3 mm. The Lagrangian speckle model estimator (LSME) was used to estimate axial strains and shears under pulsatile conditions. As anticipated, *in vitro* results showed more strain estimation artifacts with increasing magnitudes of motions in elevation. However, even with an out-of-plane motion of 2.0 mm, strain and shear estimations having inter-frame correlation coefficients higher than 0.85 were obtained. To verify findings of *in vitro* experiments, a clinical LSME dataset obtained from 18 participants with carotid artery stenosis was used. Deduced out-of-plane motions (ranging from 0.25 mm to 1.04 mm) of the clinical dataset were classified into three groups: small, moderate and large elevational motions. Clinical results showed that pulsatile time-varying strains and shears remained reproducible for all motion categories since inter-frame correlation coefficients were higher than 0.70, and normalized cross-correlations (NCC) between radiofrequency (RF) images were above 0.93. In summary, the performance of LSME axial strain and shear estimations appeared robust in the presence of out-of-plane motions (<2 mm) as encountered during clinical ultrasound imaging.

1. Introduction

The second most common death cause is stroke and it is responsible for about one in ten deaths in the world (Corbyn 2014). Atherosclerotic carotid plaque rupture is responsible for $\approx 20\%$ of ischemic stroke (Blacher *et al* 1998). Ultrasound noninvasive vascular elastography (NIVE) has shown its potential to evaluate plaque stiffness to predict plaque instability. NIVE utilizes the motion of the vessel wall caused by the natural cardiac pulsation to estimate strain fields of a plaque. Since the theoretical framework of NIVE was proposed (Maurice *et al* 2004), several noninvasive carotid strain algorithms have been developed and tested in phantom experiments, animal models or human subjects to identify vulnerable plaques (Kanai *et al* 2003, Luo and Konofagou 2011, McCormick *et al* 2012, Widman *et al* 2015, Hansen *et al* 2016, Huang *et al* 2016, Korshunov *et al* 2017, Li *et al* 2019). Hasegawa and Kanai proposed a phase-tracking method to estimate radial strain of a carotid arterial wall in longitudinal

image view (Hasegawa and Kanai 2008). Some cross-correlation-based techniques have also been used to estimate two-dimensional (2D) strain tensors (Ribbers *et al* 2007, Shi and Varghese 2007, Larsson *et al* 2011, Korukonda *et al* 2013). Recently, Porée *et al* proposed a constrained and time-ensemble approach to improve the optical flow-based Lagrangian speckle model estimator (LSME) (Porée *et al* 2015). In that report, robust 2D motion estimations in cross-sectional image view were obtained using coherent plane wave compounding (CPWC) imaging.

When 2D strain estimation is performed in cross-sectional or longitudinal image view, only in-plane motions are estimated to depict axial (along the ultrasound beam) and lateral (perpendicular to it) deformations. Since carotid wall motions are three-dimensional (3D) and periodic, they are not constrained to the imaging scan plane directions. A region of interest (ROI) may periodically be in and out of the scan plane due to vessel motion in elevation direction (i.e. perpendicular to the imaging plane); this phenomenon is known as out-of-plane motion. Brusseau *et al* (2017) assessed the influence of out-of-plane motion on quasi-static elastography by tracking a 2D ROI with a 3D search scheme. For this purpose, a specific multi-row ultrasound probe was designed to acquire three adjacent imaging planes by activating different element rows sequentially. In the field of 3D freehand breast or musculoskeletal ultrasound, speckle correlation of consecutive images was found to decrease with out-of-plane motions (Housden *et al* 2006). The elevational probe motion deduced from the speckle decorrelation has thus been used to provide probe tracking information for 3D reconstruction (Gee *et al* 2006, Laporte and Arbel 2011, Afsham *et al* 2014). For 2D NIVE, it was also hypothesized that out-of-plane motions induced estimation artifacts due to reduced image correlation. Fekkes *et al* (2016) evaluated a cross-correlation-based 2D strain estimator on a 3D atherosclerotic carotid artery simulation model considering out-of-plane motion. In that study, a longitudinal vessel motion (Cinthio *et al* 2006) was simulated and superimposed on a model mimicking out-of-plane motion for strain estimation performed in cross-sectional view. To our knowledge, the influence of out-of-plane motion on the performance of carotid artery strain estimation has not yet been evaluated experimentally.

In this study, we designed an experimental setup to simulate periodic out-of-plane motion with varying magnitudes by an oscillating linear ultrasound probe. An *in vitro* study was conducted on a diseased carotid artery phantom with a soft plaque to evaluate LSME strain performance in longitudinal and cross-sectional views. In addition, the LSME accuracy regarding different degrees of out-of-plane motion was also investigated with a clinical dataset.

2. Materials and methods

2.1. Phantom fabrication

In vitro experiments were performed on a carotid bifurcation phantom with a soft inclusion made of polyvinyl alcohol cryogel (PVA-C) material. The geometry of the phantom was based on a CT scan of a healthy volunteer (Swillens *et al* 2009). A custom made acrylonitrile butadiene styrene (ABS) mold was created by modifying the CT-scan lumen geometry to consider a 70% stenosis, using the 3D printing technology (Dimension Elite, Stratasys Inc., Eden Prairie, MN, USA). A gap between the mold and the vessel core allowed pouring a PVA-C wall thickness of 2 mm through an inlet, as shown in figure 1(a). The solution was made of 10% by weight concentration of PVA-C dissolved in pure water and mixed with 3% by weight of 50 μm cellulose particles (Sigmacell, type 50, Sigma Chemical, St. Louis, MO, USA) to provide acoustic scatterers. The PVA-C solution was injected into the mold at a temperature of 45 °C. The viscous fluid prevented cellulose particles from sinking after injection. Once injected, the molded PVA-C was immediately put inside a freezer to undergo freeze-thaw cycles, which started with a plateau at -20 °C. The thin phantom wall froze in a few minutes, which also prevented sinking of cellulose particles. The phantom wall underwent six freeze-thaw cycles at temperature characteristics defined in Fromageau *et al* (2007).

The atherosclerotic plaque mold (green part in figure 1(a)) was 1 mm smaller than the stenosis allowing the fabrication of a 1 mm thick cap of PVA-C around the soft inclusion. A second inlet (plaque inclusion inlet in figure 1(a)) was added to the mold to inject liquid PVA-C to fill the cap. The PVA-C inside the inclusion underwent 1 freeze-thaw cycle to simulate a softer plaque in the upper wall of the internal carotid artery (ICA). Young's moduli of the phantom wall and soft inclusion measured by tensile test were 342 ± 24 kPa and 17 ± 3 kPa, respectively, which is consistent with previous results (Fromageau *et al* 2007). According to reported speeds of sound and sample densities for one and six freeze-thaw cycles (Fromageau *et al* 2007), acoustic impedances of the soft inclusion and wall of the PVA-C phantom are estimated at 1.57×10^6 kg m⁻² s⁻¹ and 1.63×10^6 kg m⁻² s⁻¹, respectively. A photograph of the fabricated diseased carotid bifurcation phantom is shown in figure 1(b). Phantom dimensions are listed in table 1.

2.2. *In vitro* experimental setup

As illustrated in figure 2, the carotid bifurcation phantom was suspended in a water tank and its lumen was filled with degassed saline (5% salt) to reduce specular reflection and refraction at the phantom-liquid interface

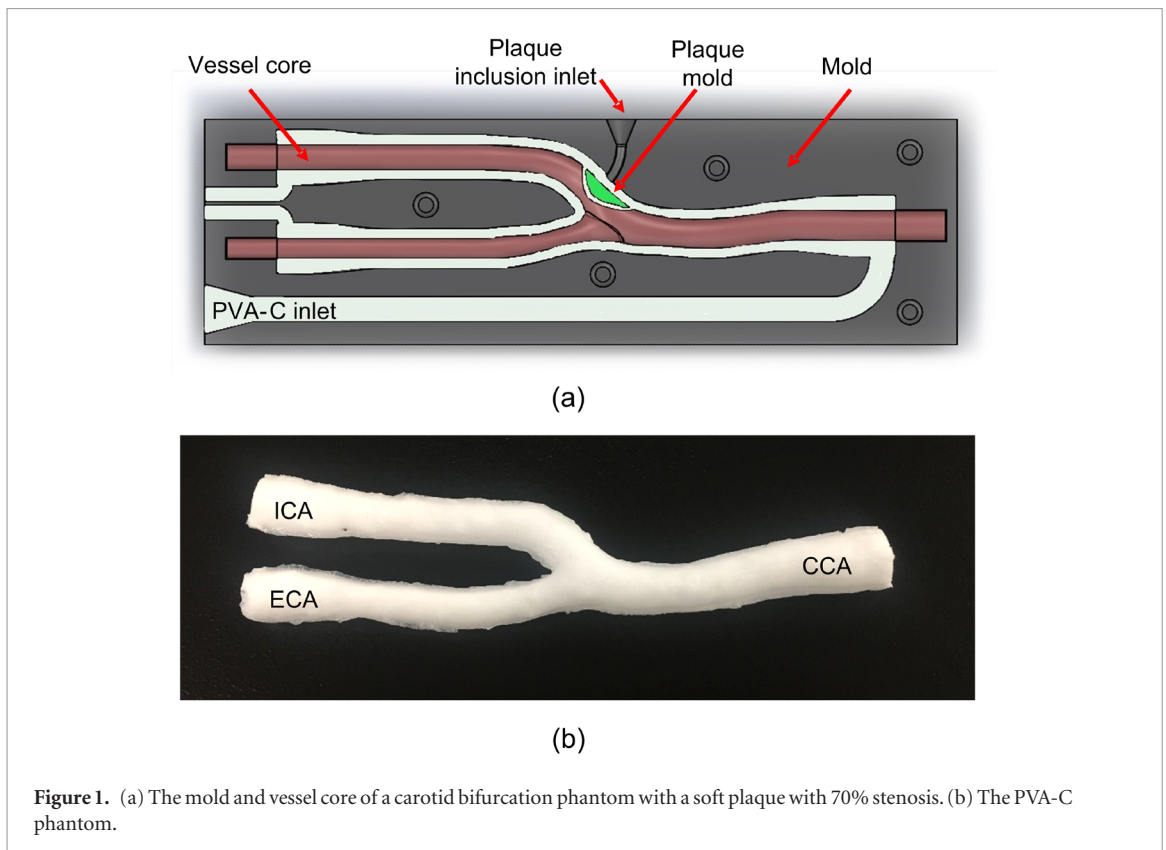


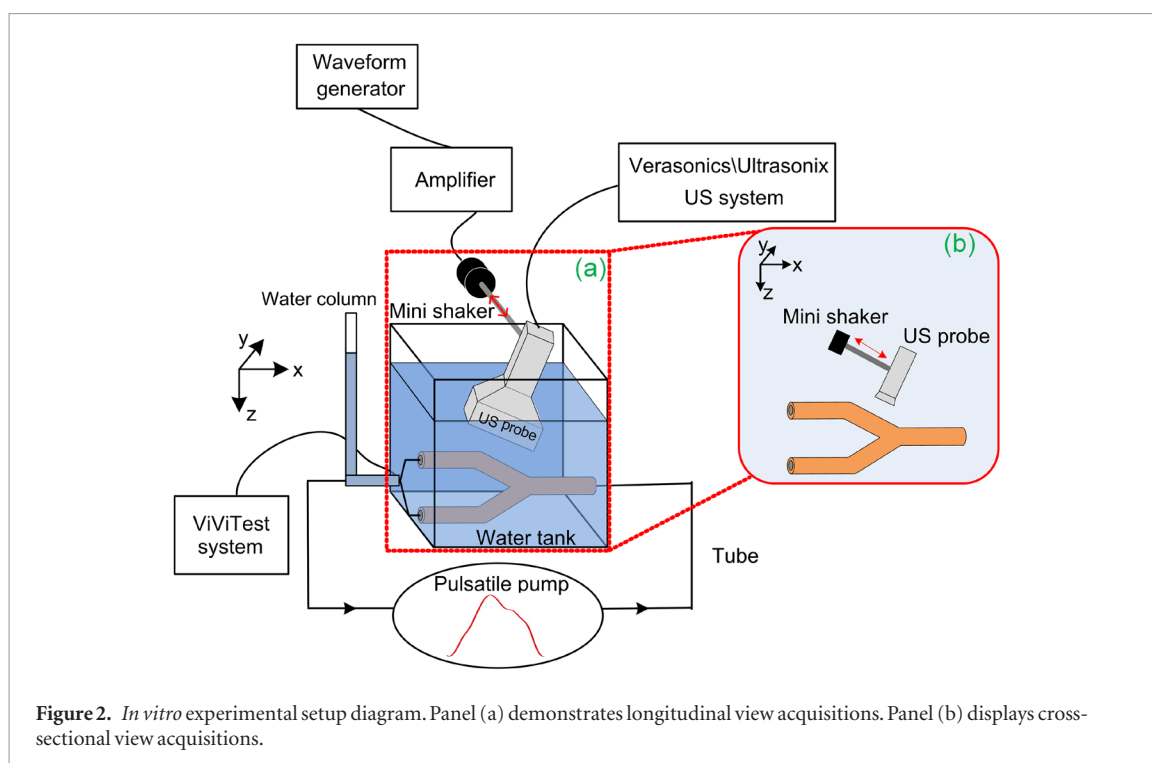
Figure 1. (a) The mold and vessel core of a carotid bifurcation phantom with a soft plaque with 70% stenosis. (b) The PVA-C phantom.

Table 1. The dimension parameters of a carotid bifurcation phantom with a soft plaque with 70% stenosis.

Dimension parameters	Dimensions
Wall thickness	2 mm
Length	123 mm
Common carotid artery (CCA) internal diameter	6 mm
ICA internal diameter	5 mm
External carotid artery (ECA) internal diameter	4 mm
Plaque size	10 mm × 4 mm

due to speed of sound differences between both media (Ribbers *et al* 2007, Hansen *et al* 2009, Porée *et al* 2015). The speed of sound in 5% saline at room temperature (25 °C) is 1550 m s⁻¹ (Kleis and Sanchez 1990), which is comparable to speeds of sound of the PVA-C material after six freeze-thaw (1550 m s⁻¹) and one freeze-thaw (1525 m s⁻¹) cycles (Fromageau *et al* 2007). The phantom ends were connected to hard inlets of the water tank to reduce longitudinal motion from the pump pulsation. Ring clamps and threads were used at both ends of the phantom to tighten the vessel and prevent leaking. The intra-luminal pressure was varied using a pulsatile pump (model 1421, Harvard Apparatus, Holliston, MA, USA) and monitored using a ViVitest software system (Vivitro Labs Inc., Victoria, BC, Canada). Maximum and minimum pressures controlled by a water column connected to the main tubing were 110 and 65 mmHg, respectively. The stroke rate of the pulsatile pump was set to 72 beats per minute to simulate the resting heart rate of an adult.

Panel (a) in figure 2 shows data acquisition in longitudinal view. A linear array transducer, whose scanning axis was parallel to the x direction of the setup, was attached to a mini-shaker (type 4810, Brüel and Kjær, Naerum, Denmark) to generate out-of-plane motions (for practical reason, we moved the probe instead of the vessel phantom). The mini-shaker was driven to vibrate as a 1.2 Hz sinusoid. The frequency and trace of the out-of-plane motion were set by a waveform generator and magnitudes of vibration were adjusted by a power amplifier (type 2706, Brüel and Kjær, Naerum, Denmark). Three out-of-plane motion magnitudes were investigated: 1 mm, 2 mm and 3 mm. The magnitudes were calibrated using a sonomicrometry system (Sonometrics Corporation, London, Ontario, Canada). Panel (b) in figure 2 presents data acquisition in cross-sectional view with the probe scanning axis parallel to the y direction. Other technical parameters were the same as longitudinal view acquisitions.



2.3. Image acquisitions and reconstructions

2.3.1. *In vitro* experiments

In vitro ultrafast plane wave data were acquired with a Verasonics research scanner (V1-128, Verasonics Inc., Redmond, WA, USA) at a sampling frequency of 20 MHz. The full aperture of a 5 MHz linear array transducer with 128 elements (ATL L7-4, Philips, Bothell, WA, USA) was used to transmit and receive plane waves, and a rectangular window apodization function was considered for beamforming. Radiofrequency (RF) data with eleven emissions between -5° to 5° with a 1° increment were beamformed using the Stolt's f - k migration (Garcia *et al* 2013), which allowed a frame rate of 400 s^{-1} . RF images were reconstructed on a regular Cartesian grid with $39 \times 75 \mu\text{m}$ (axial \times lateral) sampling distances. The duration of acquisitions was set to 2.5 s corresponding to three cycles of the pulsatile pump. There were thus 1023 frames in a whole image sequence.

2.3.2. Clinical study

To verify findings of *in vitro* experiments, we performed NIVE on a clinical dataset obtained from 18 recruited participants with carotid artery stenosis of 50% or greater. Exclusion criteria were severe vascular calcifications impeding Doppler imaging, and ICA for which there was previous radiotherapy in the neck region, endarterectomy or stenting. The study was approved by the human ethical review board of the Centre Hospitalier de l'Université de Montréal. Participants signed an informed consent.

Data acquisition details followed procedures described in previous studies (Roy Cardinal *et al* 2017, Cloutier *et al* 2018). Specifically, RF data of ICA plaques were acquired by an experienced radiologist. A Sonix ES500 RP ultrasonic system (Ultrasonix Medical Corp., Richmond, BC, Canada) equipped with a L14-5/38 linear array probe (with 128 elements and a 7.2 MHz center frequency) was used. Both longitudinal and cross-sectional scans were performed at the plaque location. We used line-by-line focused imaging instead of CPWC beamforming, as in the *in vitro* phantom study, because clinical RF data were acquired between April 2005 to December 2010 (Cloutier *et al* 2018). RF signals were sampled at 20 MHz and reconstructed on a regular Cartesian grid with $39 \times 150 \mu\text{m}$ (axial \times lateral) sampling distances. The frame rate for RF data was between 19 to 25 Hz depending on depth of ultrasound images. RF sequences were acquired for 3–5 s. During the acquisition, once the plaque imaging view was localized, the radiologist held the probe static to reduce out-of-plane motions caused by the moving probe. Moreover, participants were asked to hold breath and keep still to avoid further motions between the probe and the carotid artery.

2.3.3. Comparison of experimental conditions

An additional line-by-line focused imaging *in vitro* phantom experiment was performed using the Sonix ES500 RP scanner (L14-5/38 probe) to clarify the probe independence on reported results. Additionally, to interpret differences between *in vitro* and clinical results (explained later in Discussion), a line-by-line focused imaging experiment on phantom was performed using the Verasonics scanner (L7-4 probe) to compare with

CPWC imaging. To be consistent with the clinical study, line-by-line beamformed data in longitudinal view regarding out-of-plane motions of 1 mm, 2 mm and 3 mm were reconstructed at a resolution of $39 \times 150 \mu\text{m}$ (axial \times lateral) and a frame rate of 25 s^{-1} .

2.4. Noninvasive vascular elastography (NIVE)

To characterize complex and non-rigid plaque tissue motions, strain-based elastography was used. The optical flow based LSME (Porée *et al* 2015) is able to obtain axial strain and shear elastograms directly into a single minimization process. The optical flow model is described briefly in Appendix A and more details can be found in Porée *et al* (2015) and Li *et al* (2019). The implementation of this algorithm is briefly described here.

Firstly, contours of the vascular plaque on a single frame in the middle of the image sequence were manually drawn to generate a ROI. An automatic segmentation algorithm (Destremes *et al* 2011) was used to propagate the ROI on remaining frames. The ROI was subdivided into small measurement windows (MW). The MW size was set at $1.5 \times 1.5 \text{ mm}$ with the same 80% overlap in axial and lateral directions for *in vitro* measures, and at $1.5 \times 3 \text{ mm}$ with 95% and 90% overlaps in axial and lateral directions, respectively, for clinical data. The MW size and overlaps were kept the same as in previous clinical studies (Roy Cardinal *et al* 2017, Cloutier *et al* 2018). Secondly, a rigid registration using 2D Fourier-based ensemble-correlations (Meinhart *et al* 2000) was performed for each small MW between pre- and post-deformed RF images to account for large displacements. Then, the axial strain and shear derived from the optical flow equation were computed using a weighted least-squares method (Holland and Welsch 1977) from registered pre- and post-deformed MWs. Finally, a sequence of 2D axial strain and axial shear elastograms were used to calculate time-varying maximum and mean strain and shear curves. Only mean strains within ROIs were analyzed for the clinical dataset.

2.5. Data analysis

To evaluate the influence of *in vitro* out-of-plane motions on time-varying strain and shear curves, correlation coefficients between deformations without out-of-plane motion and different elevational motion magnitudes were computed. For example, to compute the correlation coefficient between elastography curves without out-of-plane motion (S0) and 1 mm out-of-plane motion (S1), two complete peak-to-peak cycles were selected from each curve. Elastography curve values (sampled at 400 Hz) of each cycle for S0 was used to calculate correlation coefficients with those of each cycle for S1. Thus, four correlation coefficients were obtained to compute the mean correlation coefficient and the standard deviation. The mean and standard deviation were not computed for S0 since only two cycles were available. The same procedure was used to correlate S0 with S2 (2 mm motion) and S3 (3 mm motion) acquisitions.

For the clinical study, out-of-plane motion is intrinsic due to vessel pulsation during ultrasound scan, which is impossible to determine with only 2D cross-sectional or longitudinal image view. However, for an image sequence in longitudinal view, the out-of-plane motion in elevation can be estimated by the lateral translation of a plaque ROI in cross-sectional view. This can be done with 2D block matching algorithms (Zahnd *et al* 2011, Tat *et al* 2015). In the current study, the range of cumulated lateral translation (RoCLT) for each cardiac cycle was derived by implementing such block matching method. A 2D cross-correlation-based algorithm (Zahnd *et al* 2013) considering temporal intensity variation of the reference block, using Kalman filtering, was applied on reconstructed cross-sectional B-mode images. The mean RoCLT assessed over all available cardiac cycles of a participant was averaged and considered as an estimation of the out-of-plane motion of the same plaque in the corresponding image sequence in longitudinal view. Only longitudinal elastography results of the clinical dataset are reported in this study.

Unlike *in vitro* analysis where results could be compared between different out-of-plane motions and no motion, there was no reference to compare with (i.e. no out-of-plane motion) for the clinical dataset. To assess the quality of strain estimation, two metrics were used to evaluate the reproducibility of strain curves, namely the correlation coefficient as for the *in vitro* study and the normalized cross-correlation (NCC). For the correlation coefficient, cycles of each strain curve were selected manually. Every two different cycles were used to calculate correlation coefficients. We also computed NCC between all pairs of consecutive RF images: the preceding image and the motion-compensated image, similar to Jiang *et al* (2006, 2007). Specifically, a given i th RF frame in an image sequence was warped into the $(i + 1)$ th RF frame coordinate system using the estimated 2D motion field between i th and $(i + 1)$ th frames. NCC between motion-compensated i th RF image and $(i + 1)$ th RF image was calculated for the whole image sequence. In this study, the motion compensation process consisted in an affine model considering displacements and strains from LSME estimations. The rationale behind this metric is that less out-of-plane motion between two consecutive RF frames may provide higher NCC values since more robust 2D motions were used for compensation. On the other hand, larger out-of-plane motion affecting strain estimation accuracy should be associated with smaller NCC values. Moreover, parts of strain curves associated with severe out-of-plane motion could be identified by the occurrence of small NCC values at a given time.

3. Results

3.1. Influence of out-of-plane motions on *in vitro* images in longitudinal and cross-sectional views

3.1.1. Longitudinal view image analysis

Figure 3(a) presents time-varying maximum strain curves (MaxSCs) for no motion and out-of-plane motions of 1 mm, 2 mm and 3 mm. Qualitatively, MaxSCs with 1 mm and 2 mm out-of-plane motions are similar to the curve without motion. However, it is more difficult to identify pulsatile cycles on MaxSC with 3 mm out-of-plane oscillations. Figure 3(b) shows similar results for time-varying mean strain curves (MeanSCs). Although three pulsatile cycles can be identified on MeanSC for the 3 mm out-of-plane motion, peak values are smaller than in the case of no motion. Axial strain maps superimposed on reconstructed B-mode images are shown in figures 3(c) and (d).

Figure 4 shows correlation coefficients of MaxSC and MeanSC for out-of-plane motions of 0 mm, 1 mm, 2 mm, and 3 mm. Out-of-plane motions up to 2 mm gave correlation coefficients higher than 0.9 for MaxSC. Higher correlation coefficients were obtained for MeanSCs. The general trend is a reduction of correlation coefficients with increasing out-of-plane motions. Correlation coefficient results for maximum and mean axial shears are given in appendix (figure A1).

3.1.2. Cross-sectional view image analysis

Results of time-varying MaxSCs revealed similar behavior for 0 mm and 1 mm out-of-plane motions (figure 5(a)). Although some outliers are identified for the 2 mm oscillating motion, the overall trend is also similar. By comparison, there are more outliers on MaxSC for the 3 mm out-of-plane motion, which hinders the periodicity of the strain curve. Panel (b) depicts results for time-varying MeanSCs. With 1 mm and 2 mm out-of-plane motions, results look consistent with that without motion. At 3 mm motion, it is again difficult to identify pulsatile cycles. Axial strain maps superimposed on reconstructed B-mode images are seen in figures 5(c) and (d) for two moments within a cycle.

Correlation coefficients of MaxSCs and MeanSCs for different out-of-plane motions in cross-sectional view are shown in figure 6. Overall, conclusions are similar to those reported for longitudinal view data. At the largest motion of 3 mm, MaxSCs were still severely affected as in longitudinal view; mean correlations were around 0.6. Figure A2 in Appendix shows correlation coefficients for time-varying maximum and mean shear curves in cross-sectional view.

3.2. Influence of out-of-plane motions on clinical images

In this study, the mean carotid plaque lateral displacement in cross-sectional view for 18 participants was 0.63 mm, with maximum and minimum values at 1.04 mm and 0.25 mm, respectively. Those values were considered as the anticipated out-of-plane motions in longitudinal view. We divided them into three groups, small, moderate and large out-of-plane motions, with equal range (around 0.27 mm). Examples of MeanSCs from clinical images with small, moderate and large out-of-plane motions are shown in figures 7(b), (d) and (f), respectively. Corresponding axial strain maps at peak compression of the segmented plaque superimposed on reconstructed B-mode images are presented in figures 7(a), (c) and (e). As indicated by the orange dotted line in figures 7(b), (d) and (f), NCC curves revealed higher values after dilation and compression peaks of strain curves. Figure 8 shows correlation coefficients of mean strain curves and mean NCC values for clinical data with small, moderate and large out-of-plane motions. Figure A3 presents correlation coefficients of mean shear curves and mean NCC values for the same motion categories.

3.3. Evaluation of the probe independence

Figure 4 above presented *in vitro* experimental results on axial strains using the L7-4 probe (5 MHz). To confirm that those results are not probe dependent and could be used to interpret clinical data acquired with the L14-5/38 probe (7.2 MHz), figure 9 shows correlation coefficients of MaxSC and MeanSC for different out-of-plane motions using that latter probe coupled to the Ultrasonix scanner. Similar to experiments with the L7-4 probe, both MaxSC and MeanSC were characterized by correlation coefficients higher than 0.83 for 1 and 2 mm out-of-plane motions, confirming the robustness of strain estimations.

3.4. Comparison of different beamforming strategies

Correlation coefficients of maximum and mean axial strains determined using the Verasonics scanner (L7-4 probe) for CPWC and line-by-line focused imaging beamforming are presented in figure 10. CPWC results correspond to those of figure 4. As seen, both correlation coefficients of maximum and mean strains from CPWC imaging are higher than those obtained with focused imaging.

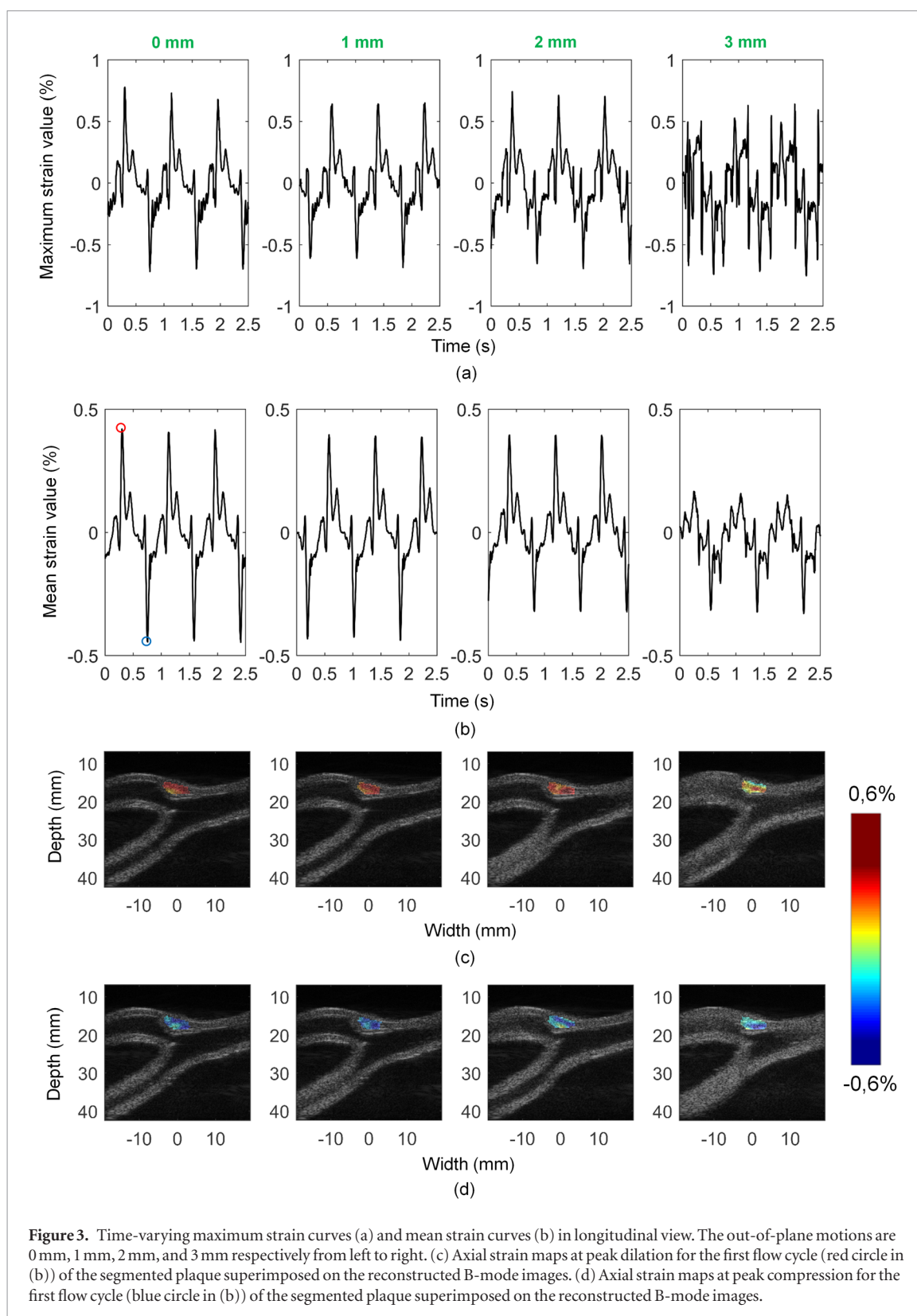


Figure 3. Time-varying maximum strain curves (a) and mean strain curves (b) in longitudinal view. The out-of-plane motions are 0 mm, 1 mm, 2 mm, and 3 mm respectively from left to right. (c) Axial strain maps at peak dilation for the first flow cycle (red circle in (b)) of the segmented plaque superimposed on the reconstructed B-mode images. (d) Axial strain maps at peak compression for the first flow cycle (blue circle in (b)) of the segmented plaque superimposed on the reconstructed B-mode images.

4. Discussion

Out-of-plane motion is unavoidable when performing 2D strain imaging due to vessel 3D displacements. Since a 1D linear array probe only provides a 2D scan plane, it is difficult to characterize motion information in elevation (i.e. outside the imaging plane). To evaluate the impact of such out-of-plane motion on strain and shear estimates with *in vitro* and clinical data, we investigated it systematically using two beamforming schemes (plane wave and focused imaging) with two linear array probes (L7-4 and L14-5/38). For *in vitro* studies, we designed an experimental setup with known motion magnitude and frequency. *In vitro* results showed that the

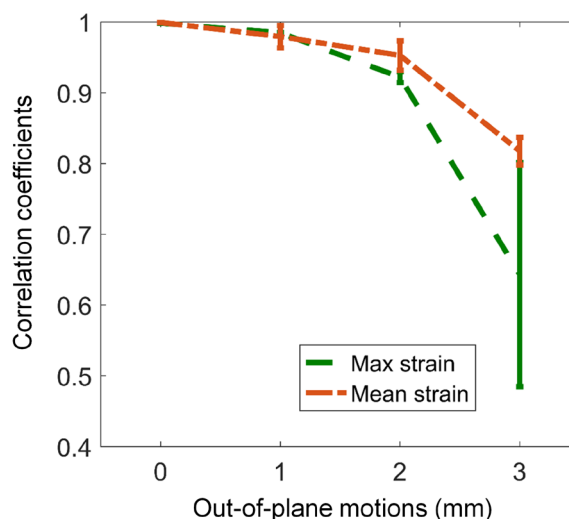


Figure 4. Correlation coefficients of time-varying maximum and mean strain curves regarding different out-of-plane motions in longitudinal view. For maximum strain curves, the correlation coefficients are 0.998, 0.985 ± 0.004 , 0.920 ± 0.008 and 0.643 ± 0.158 , respectively, for out-of-plane motions of 0 mm, 1 mm, 2 mm and 3 mm. For mean strain curves, correlation coefficients are 0.999, 0.979 ± 0.016 , 0.953 ± 0.021 and 0.818 ± 0.019 respectively for out-of-plane motions of 0 mm, 1 mm, 2 mm and 3 mm.

performance of axial strain estimations is indeed decreased with increasing out-of-plane motions. Similar results were obtained in Appendix for axial shears. Axial strain estimations with the LSME were nevertheless robust and reproducible when out-of-plane motions was ≤ 2 mm either in longitudinal or cross-sectional imaging view. For the axial shear component, mean correlation coefficients of maximum and mean shear magnitudes were above 0.87 for motions ≤ 2 mm in both longitudinal and cross-sectional imaging views.

To our knowledge, there is no study reporting clinical out-of-plane motion magnitudes because of the lack of clinical trials on carotid elastography in 3D. However, as we did in this report, out-of-plane motions can be deduced. Cinthio *et al* (2006) confirmed that the longitudinal movement of human healthy carotid artery walls had the same magnitude as the radial motion in longitudinal view, which was less than 1 mm. Recent studies showed that the longitudinal motion magnitude of carotid atherosclerotic plaques can reach 1 mm (Zahnd *et al* 2011, Tat *et al* 2016, Roy Cardinal *et al* 2017, Cloutier *et al* 2018). In the current study, we measured the maximum cumulated lateral motion of human carotid atherosclerotic plaques at 1.04 mm (mean of 0.63 ± 0.22 mm) in cross-sectional imaging view, which coincides with previous studies mentioned above. As shown *in vitro*, the performance of the LSME for axial strain and shear estimations was robust when the out-of-plane motion was 1 mm (correlation coefficients higher than 0.96), which implies that the LSME likely provides reliable axial strain and shear estimations when applied on clinical dataset.

For *in vitro* experiments, axial strain and shear estimations only had small variations between 1 mm out-of-plane motion and no motion. The elevational resolution of a linear array probe accounts for these results. It is defined by the elevational F-number = $z_f/b_h \times \lambda$, where z_f is the focal depth, b_h is the element height and λ is the transmitted pulse wavelength. For the L7-4 probe, the elevational F-number = $25/7\lambda = 1.1$ mm. The slice thickness inhibits resolving tissue structure within that range, thus reducing the impact of out-of-plane motion within the resolution cell. This explanation also applies to the clinical study, for which the elevational F-number is about 0.86 mm for the L14-5/38 probe.

From *in vivo* results in figure 7, the lowest NCC values were noticed at dilation and compression peaks of strain curves. This could be expected as these time points likely correspond to the largest magnitudes of out-of-plane motions. The potential explanation is that out-of-plane motions are synchronized with in-plane motions of the 3D carotid artery.

To properly compare reported *in vitro* and clinical results, one would need to consider the inter-frame out-of-plane motion that differed between studies. Indeed, a smaller out-of-plane motion between consecutive frames should lead to larger overlap in elevation when a 2D scan is performed, resulting in less speckle decorrelation. In the current study, although CPWC beamforming (frame rate of 400 s^{-1} , Verasonics scanner) and line-by-line focused imaging (frame rate between $18\text{--}25 \text{ s}^{-1}$, Ultrasonix scanner) were respectively used *in vitro* and in the clinical study, the mean inter-frame out-of-plane motions were smaller than $90 \mu\text{m}$. Indeed, at 400 Hz, the inter-frame out-of-plane motions of 1 mm, 2 mm and 3 mm were $6 \mu\text{m}$, $12 \mu\text{m}$ and $18 \mu\text{m}$, respectively. In the clinical study at $18\text{--}25$ Hz, mean inter-frame out-of-plane motions were $28 \mu\text{m}$, $64 \mu\text{m}$ and $90 \mu\text{m}$ for the three groups depicting different ranges of motion in elevation, respectively. Previous studies showed that when inter-frame

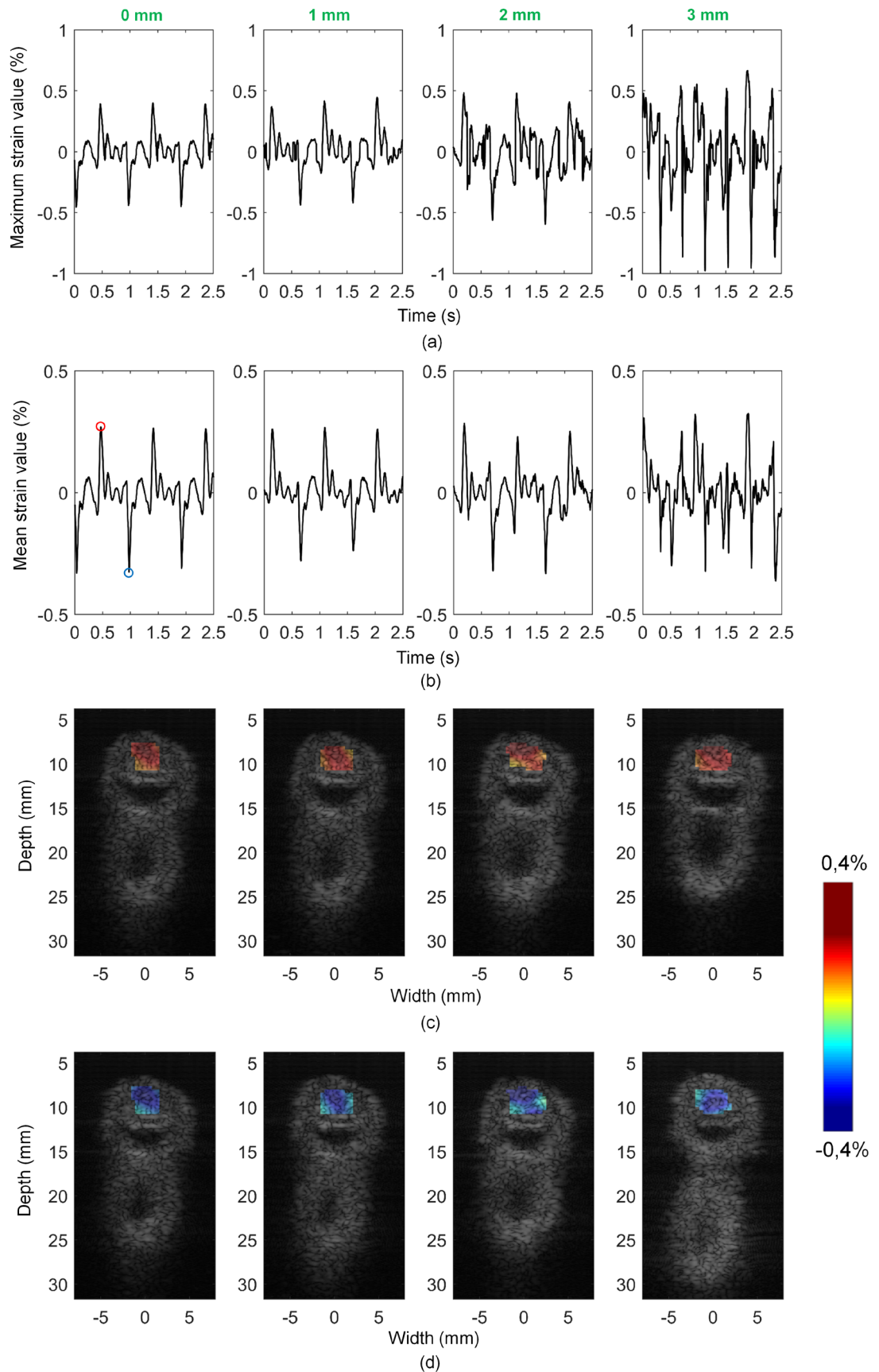


Figure 5. Time-varying maximum strain curves (a) and mean strain curves (b) in cross-sectional view. The out-of-plane motions are 0 mm, 1 mm, 2 mm and 3 mm, respectively, from left to right. (c) Axial strain maps at peak dilation for the first flow cycle (red circle in (b)) of the segmented plaque superimposed on the reconstructed B-mode images. (d) Axial strain maps at peak compression for the first flow cycle (blue circle in (b)) of the segmented plaque superimposed on the reconstructed B-mode images.

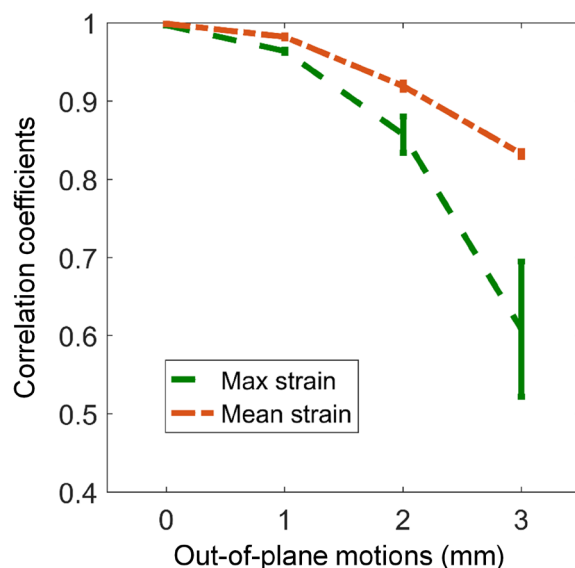


Figure 6. Correlation coefficients of time-varying maximum and mean strain curves regarding different out-of-plane motions in cross-sectional view. For maximum strain curves, the correlation coefficients are 0.997, 0.964 ± 0.002 , 0.857 ± 0.023 and 0.608 ± 0.087 , respectively, for out-of-plane motions of 0 mm, 1 mm, 2 mm and 3 mm. For mean strain curves, the correlation coefficients are 0.999, 0.982 ± 0.002 , 0.919 ± 0.005 and 0.832 ± 0.004 respectively for out-of-plane motions of 0 mm, 1 mm, 2 mm and 3 mm.

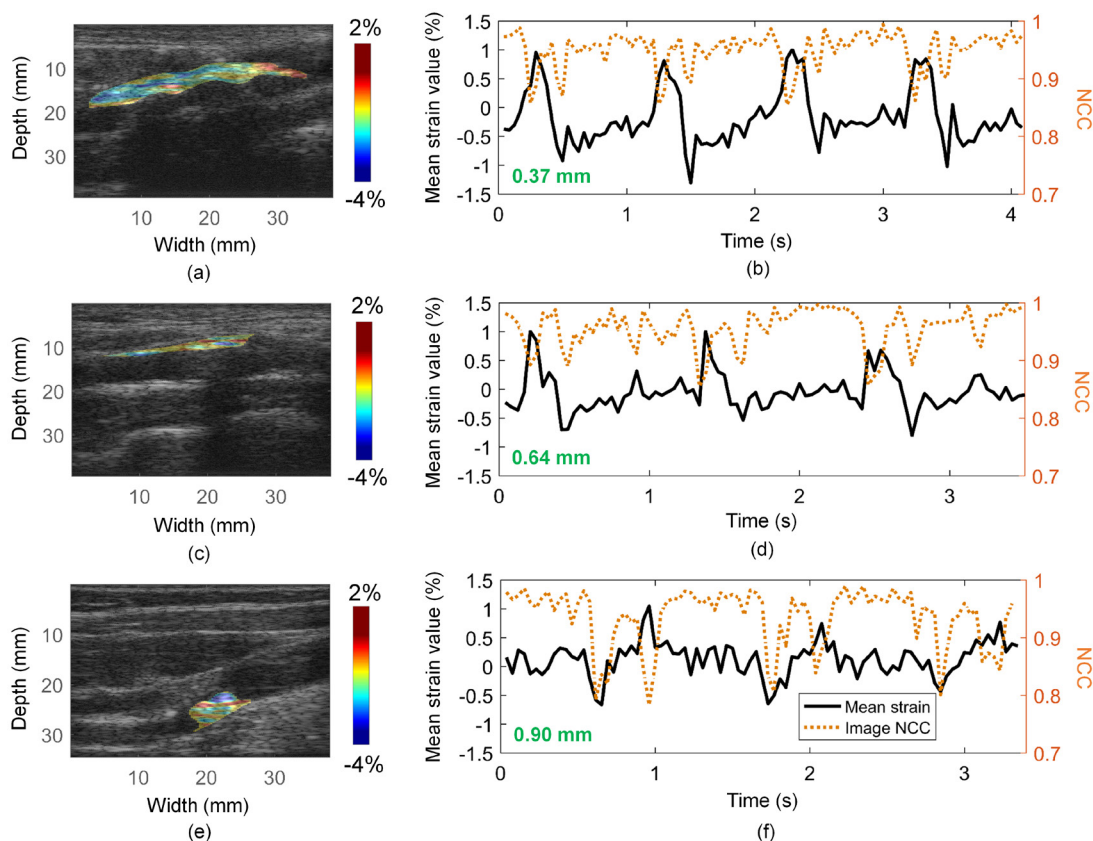


Figure 7. Examples of axial strain maps at peak compression of the segmented plaques superimposed on reconstructed B-mode images of clinical data with mean out-of-plane motions of 0.37 mm (a), 0.64 mm (c) and 0.90 mm (e). Corresponding time-varying mean strain curves and NCC curves of motion-compensated RF images (b), (d) and (f).

out-of-plane motion remains small (less than $100 \mu\text{m}$), strain estimations obtained with 2D and 3D cross-correlation-based estimators are similar (Fekkes *et al* 2016, Brusseau *et al* 2017).

As it could be seen in figure 10 with *in vitro* experiments, correlation coefficients for CPWC imaging were higher than those obtained with focused imaging when using the same ultrasound scanner (Verasonics) and

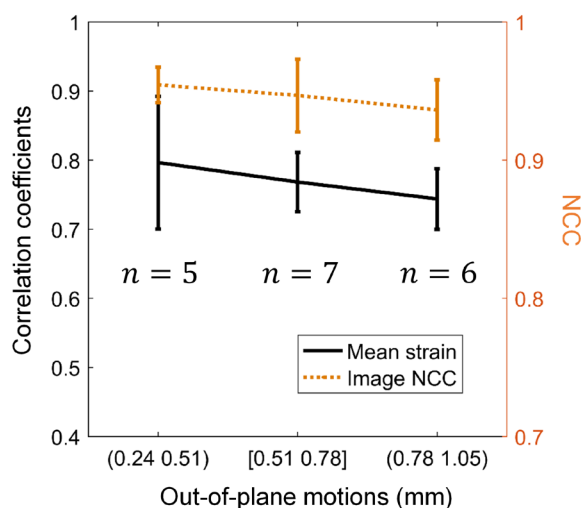


Figure 8. Correlation coefficients of mean strain curves regarding out-of-plane motion ranges of 0.24–0.51 mm, 0.51–0.78 mm, and 0.78–1.05 mm, whose sample sizes are 5, 7 and 6 participants, respectively. Correlation coefficients are 0.796 ± 0.096 , 0.768 ± 0.043 and 0.744 ± 0.044 , respectively, and corresponding mean NCC values are 0.954 ± 0.013 , 0.947 ± 0.026 and 0.936 ± 0.022 for these three groups of out-of-plane motions.

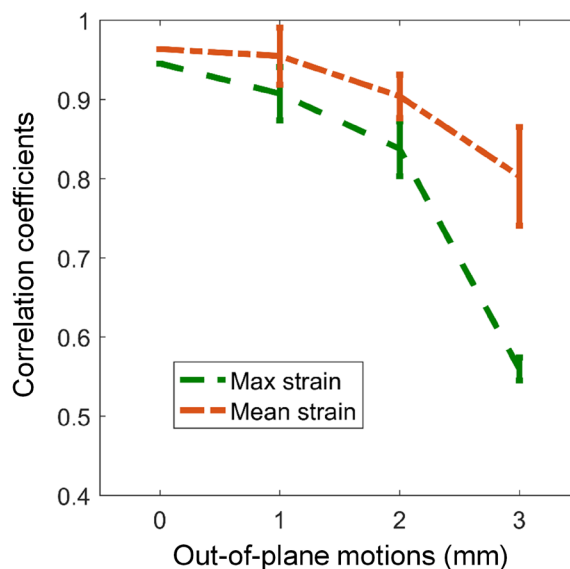


Figure 9. Correlation coefficients of time-varying maximum and mean strain curves regarding different out-of-plane motions in longitudinal view using the Ultrasonix scanner (L14-5/38 probe) for *in vitro* experiments. For maximum strain curves, correlation coefficients are 0.945, 0.907 ± 0.034 , 0.838 ± 0.035 and 0.560 ± 0.015 for out-of-plane motions of 0 mm, 1 mm, 2 mm and 3 mm, respectively. For mean strain curves, correlation coefficients are 0.964, 0.955 ± 0.036 , 0.904 ± 0.028 and 0.803 ± 0.062 for the same out-of-plane motions, respectively.

transducer (L7-4). Differences in inter-frame out-of-plane motions at frame rates of 400 s^{-1} (CPWC) versus 25 s^{-1} (focused imaging) likely accounted for this. For CPWC imaging, as mentioned above, the inter-frame out-of-plane motions for 1 mm, 2 mm and 3 mm displacements were $6 \mu\text{m}$, $12 \mu\text{m}$ and $18 \mu\text{m}$, respectively. For focused imaging, inter-frame out-of-plane motions for 1, 2 and 3 mm probe oscillation were $40 \mu\text{m}$, $80 \mu\text{m}$ and $120 \mu\text{m}$, respectively. Again, larger transverse motions resulted in more decorrelation artifacts.

Another potential factor that could cause correlation coefficient differences between *in vitro* experiments and the clinical study is the more complex human tissue structure of carotid plaques than the designed phantom. To verify that, we refer to figure 9 for the 1 mm out-of-plane motion that is within the range of the largest *in vivo* clinical out-of-plane motions (0.78–1.05 mm) of figure 8. As seen, correlation coefficients of 0.955 ± 0.036 for the *in vitro* study (at 1 mm out-of-plane motion) are higher than those of the group of patients with largest out-of-plane motions (0.744 ± 0.044). This suggests that indeed the complexity of the plaque structure contributes to decorrelation artifacts.

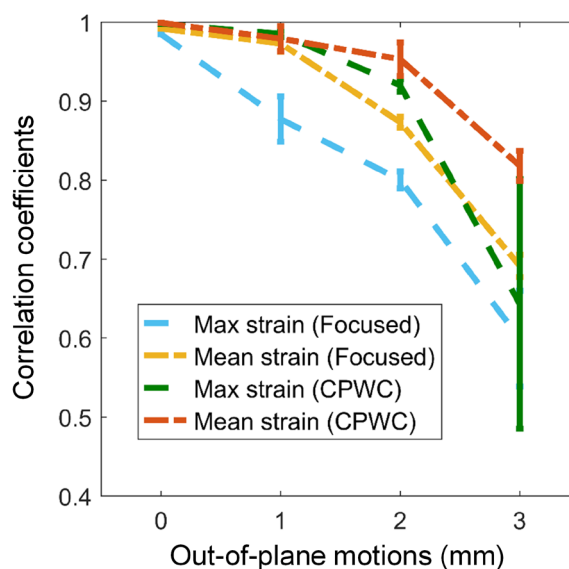


Figure 10. Correlation coefficients of time-varying maximum and mean strain curves regarding different out-of-plane motions in longitudinal view using the Verasonics scanner (L7-4 probe) with focused imaging and CPWC imaging for *in vitro* experiments considering out-of-plane motions of 0 mm, 1 mm, 2 mm and 3 mm. For maximum strain curves using focused imaging, correlation coefficients are 0.985, 0.877 ± 0.029 , 0.800 ± 0.011 and 0.599 ± 0.061 , respectively. For mean strain curves using focused imaging, correlation coefficients are 0.992, 0.973 ± 0.010 , 0.873 ± 0.007 and 0.691 ± 0.014 , respectively. For maximum and mean strain curves using CPWC imaging, correlation coefficients have been reported in figure 4.

In this study, we deduced clinical out-of-plane motions of longitudinal image sequences by using 2D cross-sectional image sequences. In the future, more accurate estimations of clinical carotid artery out-of-plane motions may be derived with 3D data using a 2D transducer array. Moreover, the 2D LSME may be extended to 3D to improve strain estimations, as theoretically derived in Maurice *et al* (2005).

5. Conclusion

In this study, the influence of out-of-plane motions on the performance of the LSME was quantified *in vitro* and evaluated clinically with atherosclerotic carotid artery plaques. The experimental framework presented in this study is of interest as it could also allow studying the impact of out-of-plane motions on other strain estimation algorithms and beamforming strategies. For *in vitro* experiments, we found higher strain and shear estimation artifacts with increasing magnitudes of out-of-plane motion (lower correlation coefficients with higher out-of-plane motions). However, even with 2.0 mm out-of-plane motion, robust axial strain and shear estimations were still obtained. The clinical study verified *in vitro* results and showed that axial strain and shear estimations with small, moderate and large out-of-plane motions were quite reproducible. This knowledge should enable more confidence when analyzing clinical dataset for vulnerable carotid atherosclerotic plaque studies. Additionally, we found that the accuracy of strain estimations was decreased with increasing inter-frame out-of-plane motions, which suggests that CPWC imaging may strengthen clinical strain assessment of carotid arteries. In conclusion, the performance of the LSME for axial strain and shear estimations is robust in the presence of out-of-plane motion magnitudes corresponding to translations of carotid artery plaques observed clinically.

Acknowledgment

This work was supported by the Collaborative Health Research Program of the Natural Sciences and Engineering Research Council of Canada (CHRP-462240-2014) and the Canadian Institutes of Health Research (CPG-134748). Clinical ultrasound data were acquired through the support of the Canadian Institutes of Health Research (PPP-78763).

Appendix A. Optical flow based LSME

Other than axial strain, the LSME is also able to provide estimations of lateral strain, and axial and lateral shears. Specifically, an affine transformation model is applied into the optical flow equation. Within a small MW with $p \times q$ pixels, an over-determined linear equation system is solved to obtain all 2D strain components.

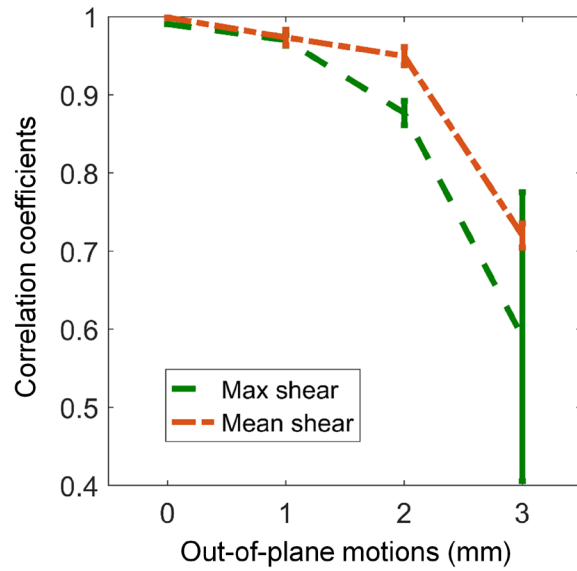


Figure A1. Correlation coefficients of maximum and mean axial shear curves regarding different out-of-plane motions in longitudinal view. For maximum shear curves, correlation coefficients are 0.991, 0.970 ± 0.007 , 0.877 ± 0.016 and 0.590 ± 0.185 respectively for out-of-plane motions of 0 mm, 1 mm, 2 mm and 3 mm. For mean shear curves, correlation coefficients are 0.999, 0.973 ± 0.010 , 0.950 ± 0.012 and 0.720 ± 0.016 , respectively, for out-of-plane motions of 0 mm, 1 mm, 2 mm and 3 mm.

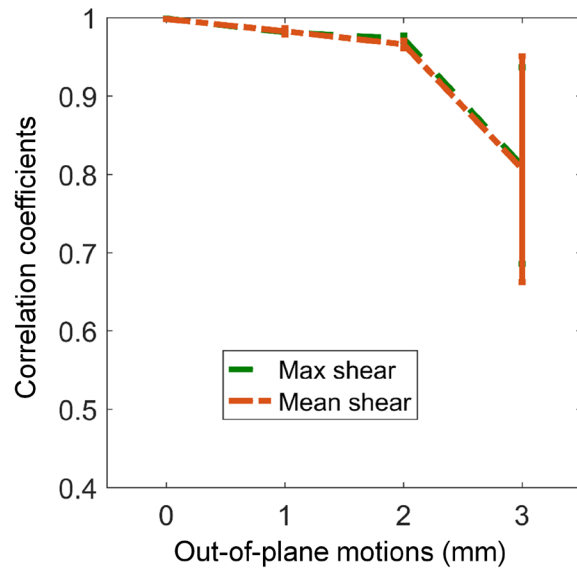
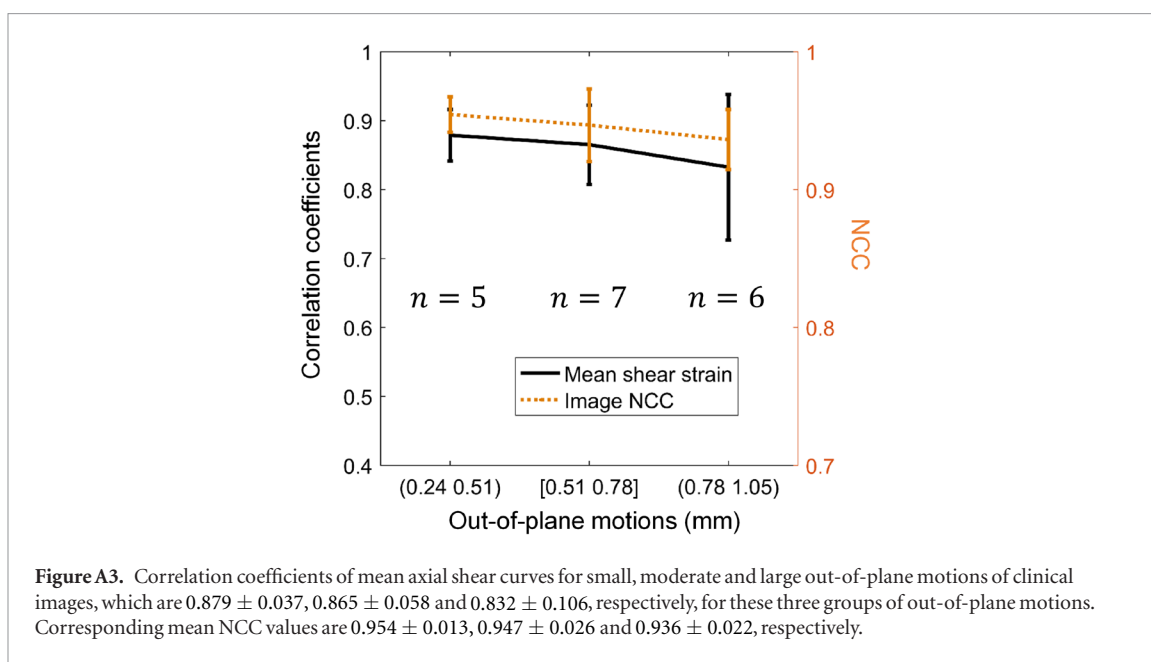


Figure A2. Correlation coefficients of maximum and mean axial shear curves regarding different out-of-plane motions in cross-sectional view. For maximum shear curves, correlation coefficients are 0.999, 0.981 ± 0.003 , 0.973 ± 0.004 and 0.811 ± 0.126 respectively for out-of-plane motions of 0 mm, 1 mm, 2 mm and 3 mm. For mean shear curves, correlation coefficients are 0.998, 0.983 ± 0.004 , 0.966 ± 0.005 and 0.807 ± 0.144 , respectively, for out-of-plane motions of 0 mm, 1 mm, 2 mm and 3 mm.

$$\begin{bmatrix} I_{x_1} x_1 & I_{x_1} z_1 & I_{x_1} & I_{z_1} x_1 & I_{z_1} z_1 & I_{z_1} \\ \vdots & \vdots & \vdots & \vdots & \vdots & \vdots \\ I_{x_p \times q} x_p \times q & I_{x_p \times q} z_p \times q & I_{x_p \times q} & I_{z_p \times q} x_p \times q & I_{z_p \times q} z_p \times q & I_{z_p \times q} \end{bmatrix} \begin{bmatrix} s_{xx} \\ s_{xz} \\ U_x \\ s_{zx} \\ s_{zz} \\ U_z \end{bmatrix} = - \begin{bmatrix} I_{t_1} \\ \vdots \\ I_{t_p \times q} \end{bmatrix}. \quad (\text{A.1})$$

where I_x, I_z are the spatial gradient of the image intensity, I_t denotes the temporal gradient of the image intensity, x, z are coordinates of pixels within the MW, $s_{xx}, s_{xz}, U_x, s_{zx}, s_{zz}, U_z$ are lateral strain, lateral shear, lateral displacement, axial shear, axial strain, and axial displacement, respectively. Here, axial strain is defined as the change in length in axial direction divided by the initial length in axial direction. Correspondingly, axial shear is defined as the change in length in axial direction divided by the initial length in lateral direction. In the current



study, because of the limited lateral resolution of ultrasound imaging, lateral strain and shear components were not analyzed.

Appendix B. Decorrelation results for the axial shear component

Figure A1 shows correlation coefficients of maximum and mean axial shear curves for out-of-plane motions of 0 mm, 1 mm, 2 mm, and 3 mm for *in vitro* longitudinal view images. Figure A2 presents the same results in cross-sectional view. Finally, figure A3 shows correlation coefficients of mean axial shear curves for small, moderate and large out-of-plane motions for the clinical dataset. As done in previous studies (Roy Cardinal *et al* 2017, Cloutier *et al* 2018), the absolute shear magnitude averaged within the segmented area was considered for maximum and mean time-varying curves.

ORCID iDs

Richard G P Lopata  <https://orcid.org/0000-0001-6618-6184>

Guy Cloutier  <https://orcid.org/0000-0002-4957-4844>

References

- Afsham N *et al* 2014 A generalized correlation-based model for out-of-plane motion estimation in freehand ultrasound *IEEE Trans. Med. Imaging* **33** 186–99
- Blacher J *et al* 1998 Carotid arterial stiffness as a predictor of cardiovascular and all-cause mortality in end-stage renal disease *Hypertension* **32** 570–4
- Brusseau E *et al* 2017 Specific ultrasound data acquisition for tissue motion and strain estimation: Initial results *Ultrasound Med. Biol.* **43** 2904–13
- Cinthio M *et al* 2006 Longitudinal movements and resulting shear strain of the arterial wall *Am. J. Physiol. Heart Circ. Physiol.* **291** H394–402
- Cloutier G *et al* 2018 Carotid plaque vulnerability assessment using ultrasound elastography and echogenicity analysis *Am. J. Roentgenol.* **211** 847–55
- Corbyn Z 2014 Stroke: a growing global burden *Nature* **510** 5–6
- Destrempe F *et al* 2011 Segmentation of plaques in sequences of ultrasonic B-mode images of carotid arteries based on motion estimation and a Bayesian model *IEEE Trans. Biomed. Eng.* **58** 2202–11
- Fekkes S *et al* 2016 2D versus 3D cross-correlation-based radial and circumferential strain estimation using multiplane 2D ultrafast ultrasound in a 3D atherosclerotic carotid artery model *IEEE Trans. Ultrason. Ferroelectr. Freq. Control* **63** 1543–53
- Fromageau J *et al* 2007 Estimation of polyvinyl alcohol cryogel mechanical properties with four ultrasound elastography methods and comparison with gold standard testings *IEEE Trans. Ultrason. Ferroelectr. Freq. Control* **54** 498–508
- Garcia D *et al* 2013 Stolt's *s-f-k* migration for plane wave ultrasound imaging *IEEE Trans. Ultrason. Ferroelectr. Freq. Control* **60** 1853–67
- Gee A H *et al* 2006 Sensorless freehand 3D ultrasound in real tissue: speckle decorrelation without fully developed speckle *Med. Image Anal.* **10** 137–49
- Hansen H H G *et al* 2016 Validation of noninvasive *in vivo* compound ultrasound strain imaging using histologic plaque vulnerability features *Stroke* **47** 2770–5
- Hansen H H G, Lopata R G P and de Korte C L 2009 Noninvasive carotid strain imaging using angular compounding at large beam steered angles: validation in vessel phantoms *IEEE Trans. Med. Imaging* **28** 872–80

- Hasegawa H and Kanai H 2008 Simultaneous imaging of artery-wall strain and blood flow by high frame rate acquisition of RF signals *IEEE Trans. Ultrason. Ferroelectr. Freq. Control* **55** 2626–39
- Holland P W and Welsch R E 1977 Robust regression using iteratively reweighted least-squares *Communi. Stat. Theory Methods* **6** 813–27
- Housden R J et al 2006 Sub-sample interpolation strategies for sensorless freehand 3D ultrasound *Ultrasound Med. Biol.* **32** 1897–904
- Huang C et al 2016 Ultrasound-based carotid elastography for detection of vulnerable atherosclerotic plaques validated by magnetic resonance imaging *Ultrasound Med. Biol.* **42** 365–77
- Jiang J, Hall T J and Sommer A M 2006 A Novel performance descriptor for ultrasonic strain imaging: a preliminary study *IEEE Trans. Ultrason. Ferroelectr. Freq. Control* **53** 1088–102
- Jiang J, Hall T J and Sommer A M 2007 A novel image formation method for ultrasonic strain imaging *Ultrasound Med. Biol.* **33** 643–52
- Kanai H et al 2003 Elasticity imaging of atheroma with transcutaneous ultrasound: preliminary study *Circulation* **107** 3018–21
- Kleis S J and Sanchez L A 1990 Dependence of speed of sound on salinity and temperature in concentrated NaCl solutions *Sol. Energy* **45** 201–6
- Korshunov V A et al 2017 Model-based vascular elastography improves the detection of flow-induced carotid artery remodeling in mice *Sci. Rep.* **7** 1–12
- Korukonda S et al 2013 Noninvasive vascular elastography using plane-wave and sparse-array imaging *IEEE Trans. Ultrason. Ferroelectr. Freq. Control* **60** 332–42
- Laporte C and Arbel T 2011 Learning to estimate out-of-plane motion in ultrasound imagery of real tissue *Med. Image Anal.* **15** 202–13
- Larsson M et al 2011 Ultrasound-based radial and longitudinal strain estimation of the carotid artery: A feasibility study *IEEE Trans. Ultrason. Ferroelectr. Freq. Control* **58** 2244–51
- Li H et al 2019 Two-dimensional affine model-based estimators for principal strain vascular ultrasound elastography with compound plane wave and transverse oscillation beamforming *Ultrasonics* **91** 77–91
- Luo J and Konofagou E E 2011 Imaging of wall motion coupled with blood flow velocity in the heart and vessels *in vivo*: a feasibility study *Ultrasound Med. Biol.* **37** 980–95
- Maurice R L et al 2004 Noninvasive vascular elastography: theoretical framework *IEEE Trans. Med. Imaging* **23** 164–80
- Maurice R L et al 2005 Non-invasive high-frequency vascular ultrasound elastography *Phys. Med. Biol.* **50** 1611–28
- McCormick M et al 2012 Methods for robust *in vivo* strain estimation in the carotid artery *Phys. Med. Biol.* **57** 7329–53
- Meinhart C D, Wereley S T and Santiago J G 2000 A PIV algorithm for estimating time-averaged velocity fields *J. Fluids Eng.* **122** 285–9
- Porée J et al 2015 Non-invasive vascular elastography with plane strain incompressibility assumption using ultrafast coherent compound plane wave imaging *IEEE Trans. Med. Imaging* **34** 2618–31
- Ribbers H et al 2007 Noninvasive two-dimensional strain imaging of arteries: validation in phantoms and preliminary experience in carotid arteries *in vivo* *Ultrasound Med. Biol.* **33** 530–40
- Roy Cardinal M-H et al 2017 Carotid artery plaque vulnerability assessment using noninvasive ultrasound elastography: validation with MRI *Am. J. Roentgenol.* **209** 142–51
- Shi H and Varghese T 2007 Two-dimensional multi-level strain estimation for discontinuous tissue *Phys. Med. Biol.* **52** 389–401
- Swillens A et al 2009 Ultrasound simulation of complex flow velocity fields based on computational fluid dynamics *IEEE Trans. Ultrason. Ferroelectr. Freq. Control* **56** 546–56
- Tat J et al 2015 Reduced common carotid artery longitudinal wall motion and intramural shear strain in individuals with elevated cardiovascular disease risk using speckle tracking *Clin. Physiol. Funct. Imaging* **37** 106–16
- Tat J, Psaromiligkos I N and Daskalopoulou S S 2016 Carotid atherosclerotic plaque alters the direction of longitudinal motion in the artery wall *Ultrasound Med. Biol.* **42** 2114–22
- Widman E et al 2015 Ultrasound speckle tracking strain estimation of *in vivo* carotid artery plaque with *in vitro* sonomicrometry validation *Ultrasound Med. Biol.* **41** 77–88
- Zahnd G et al 2011 Measurement of two-dimensional movement parameters of the carotid artery wall for early detection of arteriosclerosis: a preliminary clinical study *Ultrasound Med. Biol.* **37** 1421–9
- Zahnd G et al 2013 Evaluation of a Kalman-based block matching method to assess the bi-dimensional motion of the carotid artery wall in B-mode ultrasound sequences *Med. Image Anal.* **17** 573–85